

Cosmic-ray yield and response functions in the atmosphere

R. A. Caballero-Lopez¹ and H. Moraal²

Received 4 April 2012; revised 12 September 2012; accepted 22 October 2012; published 13 December 2012.

[1] Since the middle 1950s, neutron monitors have provided a continuous record of the intensity of secondary atmospheric particles produced by the primary cosmic radiation above the atmosphere. The number of counts due to these secondary particles is related to the primary spectrum above the atmosphere through the so-called atmospheric yield function. This yield function includes the secondary particles produced in the atmosphere, as well as inside the particular detector. In this paper the primary focus is to recalculate the yield function for neutron monitors. The motivation for this study is that the quality of the experimental observations has increased to such an extent that it has become possible to reduce uncertainties in the yield function down to approximately 10%. It thus becomes possible to refine our knowledge of the atmospheric cascade process considerably. We parameterize the yield functions in a simple way; we also make reference to the yield and response functions of muon, Cherenkov and stratospheric balloon detectors, and we compare their response to that of the neutron monitors.

Citation: Caballero-Lopez, R. A., and H. Moraal (2012), Cosmic-ray yield and response functions in the atmosphere, *J. Geophys. Res.*, 117, A12103, doi:10.1029/2012JA017794.

1. Introduction

[2] Cosmic rays that arrive at the top of the atmosphere are called primaries. When they subsequently penetrate the atmosphere they produce showers of secondary particles such as neutrons, protons, muons and pions, plus an electromagnetic shower. These secondary particles are detected by instruments inside the atmosphere, mainly on ground level, but also with sub-surface detectors, and high up in the atmosphere with aircraft and balloons. The relationship between the intensity of primary cosmic rays and the counting rate of an instrument inside the atmosphere is called the atmospheric yield function for that particular instrument. Mathematically the process is described as follows: the counting rate $\dot{N}(P_c, x, t)$ of a detector at cutoff rigidity P_c , atmospheric depth x and time t is such that

$$\dot{N}(P_c, x, t) = \int_{P_c}^{\infty} (-dN/dP) dP = \sum_i \int_{P_c}^{\infty} S_i(P, x) j_i(P, t) dP, \quad (1)$$

where $j_i(P, t)$ is the spectrum of the primary species i above the atmosphere, and $S_i(P, x)$ is the atmospheric yield function due to this species. The cutoff rigidity of a position on Earth (or anywhere inside the geomagnetosphere) is the minimum

rigidity that a primary cosmic ray must have to reach that point, or to produce secondaries that can reach it. The quantity $-dN/dP$ is the differential counting rate of the instrument inside the atmosphere. It is often called the differential response function of the detector. However, this name should be reserved for the related quantity $-d \ln N/dP$, which is the fractional contribution per unit rigidity to the counting rate of the detector. In this work, the quantity $-dN/dP$ is called the neutron monitor differential counting rate. Note that dN/dP and $d \ln N/dP$ are negative because the counting rate in (1) decreases with rigidity.

[3] There are basically two ways to determine the atmospheric yield function S . The experimental or empirical way is to simultaneously measure the counting rate of an instrument inside, and the primary spectrum outside the atmosphere. Numerous papers have been published on this method, with the latest ones we are aware of by *Nagashima et al.* [1989], *Moraal et al.* [1989], *Bieber et al.* [1997], and *Dorman et al.* [2000]. These results and many others are comprehensively reviewed and summarized in the book of *Dorman* [2009]. The other method is to calculate the yield function by using one of several generic numerical codes such as FLUKA, GEANT4 and CORSIKA (KASKADE) to simulate the atmospheric cascade process, and then adding detector-specific details to these models. This approach is comprehensively summarized by *Clem and Dorman* [2000], and later by *Bazilevskaya et al.* [2008].

[4] In this paper we show that unprecedented accurate measurements of primary cosmic-ray Hydrogen and Helium spectra in the period 2006 to 2008 enable us to derive an empirical yield function for neutron monitors with significantly higher accuracy than before. When empirically and theoretically derived yield functions in this rigidity range are compared, the typical differences are of the order of a factor

¹Ciencias Espaciales, Instituto de Geofísica, Universidad Nacional Autónoma de México, Mexico City, Mexico.

²Centre for Space Research, School of Physical and Chemical Sciences, North-West University, Potchefstroom, South Africa.

Corresponding author: R. A. Caballero-Lopez, Ciencias Espaciales, Instituto de Geofísica, Universidad Nacional Autónoma de México, Mexico City, 04510 México D.F., México. (rogelioc@geofisica.unam.mx)

©2012. American Geophysical Union. All Rights Reserved.
0148-0227/12/2012JA017794

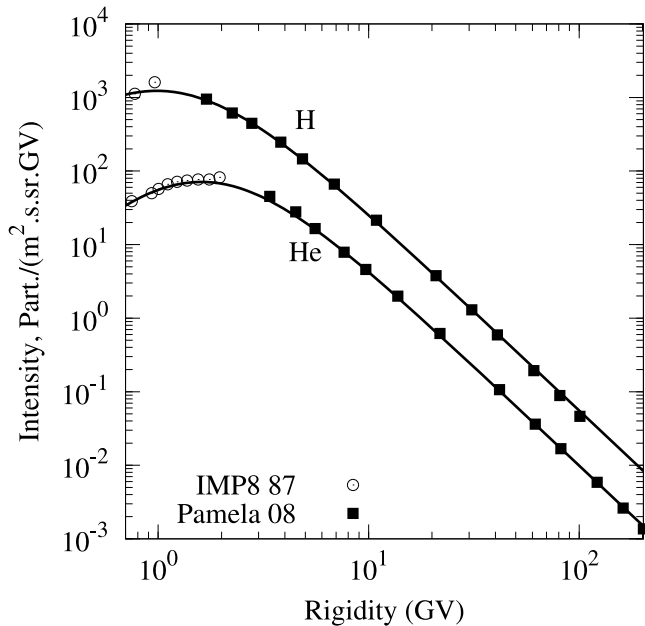


Figure 1. Hydrogen and Helium intensity spectra in 2006–2008 and 1987 as a function of rigidity. Pamela data points are from *Adriani et al.* [2011] and IMP8 data are from *Caballero-Lopez et al.* [2004]. The fit to the data is a double power law described by (2) with coefficients in the first two lines of Table 1. The reduced chi-squared (chi-squared divided by the degrees of freedom) values are 1.10 for H and 1.18 for He. These spectra are representative for the $qA < 0$ cosmic-ray maximum in 1987.

of 2. This error margin reflects remaining inaccuracies of the secondary production processes in the numerical codes. Second, we introduce a simple parameterization of this yield function. Third, we extend our calculations to muon telescopes, Cherenkov detectors, and the Russian balloon-borne stratospheric detector described in *Stozhkov et al.* [2009]. Finally, in the last section, we calculate the neutron monitor response to solar energetic particles, and show the resulting spectra and counting rates of ground-level enhancements due to these particles.

2. The Basic Data Sets

[5] The two basic experimental data sets for this paper are (a) the Pamela measurements of cosmic-ray Hydrogen and Helium spectra in the vicinity of Earth during the years

2006, 2007 and 2008, supplemented by IMP8 measurements in 1987, and (b) a neutron monitor latitude survey at sea level during 1987. We will show that these observations are well representative of the cosmic-ray intensity during the solar minimum of the 1986/1987 epoch, in which the cosmic-ray intensity peaked in March 1987.

[6] The Hydrogen and Helium spectra are shown in Figure 1. They are a compound of Pamela observations at rigidity $P > 1$ GV for H, and at $P > 3$ GV for He, together with IMP8 spectra below these rigidities. The Pamela spectra are for the period July 2006 until March 2008, with December 2006 excluded because there was significant modulation during that month. The observations are from *Adriani et al.* [2011]. These Pamela observations were more than a year before the solar minimum of 2009, but it is well-observed that during this minimum the cosmic-ray intensity was significantly higher than during the 1987 minimum, [e.g., *Moraal and Stoker*, 2010]. The IMP8 observations are for the period February to October 1987, and are taken from *Caballero-Lopez et al.* [2004].

[7] In this paper we use a double power law to parameterize our spectra and several other functions. We find this a useful parameterization. The formula is

$$F(P) = F_0(P_0^a + P^a)^{(\gamma_1 - \gamma_2)/a} P^{\gamma_2}. \quad (2)$$

When $P \gg P_0$ the function F is a power law of the form $F \propto P^{\gamma_1}$, while for $P \ll P_0$ it is $F \propto P^{\gamma_2}$. The parameter $a > 0$ determines the sharpness of the transition from power-law index γ_1 to γ_2 : when $a \gg 1$ the transition is sharp, and it becomes smoother as a decreases. The first two lines of Table 1 give the values of the five parameters F_0 , P_0 , a , γ_1 and γ_2 for the fits drawn in Figure 1. The power-law index $\gamma_1 = -2.7$ agrees with that reported by *Webber and Lockwood* [2001], *Webber and Higbie* [2010] and *Gaisser and Stanev* [2010], while *Moskalenko et al.* [2002] report γ_1 somewhere between -2.7 and -2.8 . Care should be taken not to use this fit below its limit of validity at $P = 0.7$ GV (shown in the last column of Table 1). For the parameter fitting throughout this paper we use the non-linear least-squares Marquardt-Levenberg algorithm.

[8] The second set of observations is that of neutron monitor counting rates measured inside the atmosphere, primarily at sea level. Figure 2 shows the results of the sea-level neutron monitor latitude survey of *Moraal et al.* [1989], conducted on three vessels during the period June 1986 to October 1987. The data points are average intensities in 0.25 GV intervals of cutoff rigidity P_c . This average

Table 1. Parameters for the Double Power-Law Functions of the Form (2) Used in This Work^a

Function	F_0	$P_0(\text{GV})$	a	γ_1	γ_2	Rigidity Range (GV)
Spectrum	$\left(\frac{\text{primaries}}{\text{m}^2 \cdot \text{s} \cdot \text{sr} \cdot \text{GV}}\right)$					
H	14000	0.96	1.5	-2.7	2.8	$0.7 < P < 10^4$
He	2500	1.5	1.6	-2.7	3.0	$0.7 < P < 10^4$
H Yield Function	$\left(\frac{\text{m}^2 \cdot \text{sr}}{\text{primary}}\right)$					
CD00	2.0×10^{-4}	0.45	1.4	0.89	30.0	$1.0 < P < 10^3$
This work	2.0×10^{-4}	2.0	1.45	0.89	7.7	$1.0 < P < 10^3$
GRAND MT	1.07×10^{-3}	1.0	1.0	0.85	28.0	$1.7 < P < 10^3$
IceTop	1.68×10^{-4}	1.0	1.0	1.16	12.5	$0.7 < P < 10^3$
He/H Yield NM	2.0	0.45	1.4	0	10.0	$1.0 < P < 10^3$

^aCD00 is from *Clem and Dorman* [2000], and GRAND MT is for a muon telescope from *Poirier and D'Andrea* [2002].

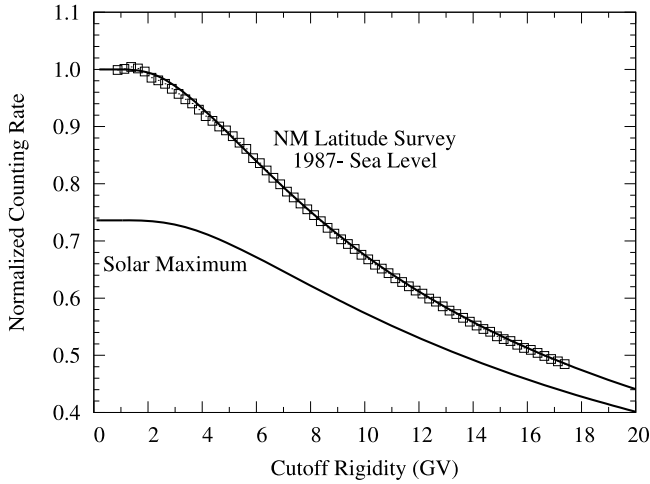


Figure 2. Neutron monitor counting rates in 1987 from *Moraal et al.* [1989]. The fit to the data points is the Dorman function described by equation (3) with the parameters in the third line of Table 2. The bottom line shows the typical solar maximum counting rate, calculated for June 1991 using the modulation function given in (22) and the parameters in Table 2.

implies that the data of one to three vessels may be included in a particular cutoff rigidity interval, and for each vessel there can be several passes through this interval, both in the northern and southern hemispheres. The vertical height of the data boxes is an estimate of the combined statistical and systematic error.

[9] The neutron monitor counting rates in this paper are parameterized with the well-known Dorman function [*Dorman et al.*, 1970], given by

$$N(P_c) = N_0 [1 - \exp(-\alpha P_c^{-k})] \quad (3)$$

The parameters for the 1987 counting rate in Figure 2 are given in the third line of Table 2. The flat portion of the

counting rate at low rigidities is due to the fact that the geomagnetic cutoff becomes smaller than the atmospheric cutoff of ≈ 1 GV. Note that the accuracy of this fit is higher than the combined statistical and systematic error on the data, but that beyond 15 GV the curve is a pure extrapolation because there are no neutron monitors with cutoff rigidities above this rigidity.

[10] In order to derive accurate atmospheric yield functions, it is important that the measurements in space and in the atmosphere must be taken at the same time, or at least during periods when the cosmic-ray intensity is comparable. Such simultaneous observations are difficult to find, but the three data sets used here are well-suited for this criterion. We noted the absolute level of the cosmic-ray intensity during these three observational periods by using the Hermanus neutron monitor counting rates, from <http://www.nwu.ac.za/neutron-monitor-data>. The ratio of these counts during the Pamela observational period relative to the IMP8 period was $\text{Pamela-06-08/IMP8-87} = 0.990$. Similarly, the ratio relative to the neutron monitor latitude survey is $\text{Pamela-06-08/NM-87} = 0.986$, and from these two ratios it follows that the counting ratio for the IMP8 and neutron monitor periods is $\text{IMP8-87/NM-87} = 0.996$. This means that the neutron monitor intensities during the Pamela period were about 1% lower than during the IMP8 period, and 1.5% lower than in the latitude survey period. We have corrected for these differences as follows: In the simplest convection-diffusion description of the modulation, modulation changes in the intensity j are given by $\delta j/j = 1 - \exp[\delta m/(\beta P)]$. If $\delta m = \pm 0.13$ and P is expressed in units of GV, this causes a variation in the primary spectra and dN/dP of $\pm 16\%$ at 1 GV, a variation of a polar neutron monitor counting rate at $P_c < 1$ GV of $\pm 1.4\%$, and a variation of $\pm 1.0\%$ in the Hermanus counting rate at $P_c = 5$ GV. We have therefore corrected the yield function with $\delta m = +0.13$, i.e. increased it with 16% at 1 GV. If we further assume that neutron monitor counting rates at $P_c < 1$ GV contain a

Table 2. Parameters for the Spectra and Response Functions Used in This Work^a

Quantity/Instrument	α	k	$P_{\max,s} - (1/N_0)$ (dN/dP) _{max}		$P_{\max,r}$ ($-d \ln N/dP$) _{max}		P_{med} ($P_c = 1$ GV) GV	P_{med} ($P_c = 15$ GV) GV
			GV	%/GV	GV	%/GV		
Neutron monitor:								
Nominal SL (solar min.)	9.50	0.93	5.1	4.7	6.4	5.6	16.7	39.5
1976 qA > 0 SL	8.953	0.916	4.9	4.8	6.1	5.8	16.3	39.9
1987 qA < 0 SL (calculated)	10.068	0.952	5.3	4.7	6.6	5.5	16.6	38.6
1976 qA > 0 30 000 ft	7.990	1.215	3.4	10.6	4.3	13.1	7.5	28.3
1987 qA < 0 30 000 ft	9.107	1.251	3.7	10.2	4.7	12.9	7.8	27.8
Nominal SL (solar max.)	12.85	0.93	7.1	3.4	8.8	4.0	23	43
Stratospheric detector:								
qA < 0 300 g/cm ²	8.665	0.890	4.9	4.7	5.9	5.0	17.1	41.4
qA < 0 100 g/cm ²	5.576	1.003	2.8	9.7	3.5	11.7	8.0	33.0
qA < 0 40 g/cm ²	4.643	1.037	2.3	12.5	2.9	15.2	6.3	31.4
qA < 0 SL (calculated)	20.06	0.474	51	0.1	58	0.1	>1000	>1000
GRAND MT 1005 g/cm ²	23.56	0.906	14.4	1.6	17.8	1.9	49.0*	-
IceTop 700 g/cm ²	11.2	0.76	7.96	2.2	9.6	2.4	38.9	-
GLEs for sea level NMs:								
Spectrum $\sim P^{-4}$	4.791	1.49	2.03	23.2	2.6	29.8	3.68	24.2
Spectrum $\sim P^{-5}$	3.467	1.92	1.54	41.4	2.0	57.8	2.37	21.6
Spectrum $\sim P^{-6}$	2.436	2.40	1.25	65.8	1.6	94.2	1.78	20.0

^aThe neutron monitor values for 1987 at 30 000 ft are not measured, but calculated from (21) and the measured altitude dependence in 1976. Note: 30 000 ft corresponds an atmospheric depth of 307 g/cm² and sea level (SL) to 1033 g/cm². * For $P_c = 1.9$ GV.

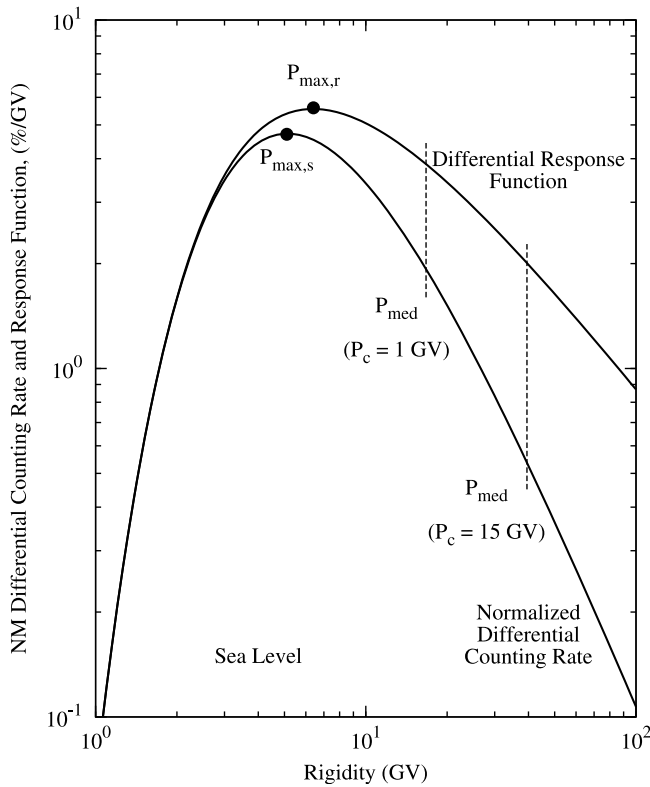


Figure 3. Neutron monitor normalized differential counting rate from (4) and differential response function from (8) at sea level. The nominal values of $\alpha = 9.50$ and $k = 0.93$ in the first line of Table 2 were used.

remaining uncertainty of $\pm 1.0\%$, as was found, for instance, in *Moraal and Stoker* [2010], then the resulting error band in the yield function is shown by the two dashed lines in Figure 5 (bottom).

3. Parameterization of Neutron Monitor Differential Counting Rate and Response Function

[11] The second line of Table 2 gives the parameters for a similar latitude survey at sea level conducted by *Potgieter et al.* [1980] during the 1976 solar minimum. This survey was conducted in the so-called $qA > 0$ drift cycle, while the 1987 survey was conducted in the $qA < 0$ cycle. As described in *Moraal et al.* [1989], one expects these spectra to be different during these periods. From these two surveys it follows that good, nominal or average values of the two parameters in the Dorman function (3) at sea level are $\alpha = 9.5$ and $k = 0.93$. This produces a differential response function halfway between the $qA > 0$ and $qA < 0$ response functions. The spectral properties for these nominal values are shown in the first line of Table 2.

[12] The derivative of (3) gives the differential neutron monitor counting rate:

$$-dN/dP = \alpha k N_0 \exp(-\alpha P^{-k}) P^{-k-1} = \alpha k (N_0 - N) P^{-k-1}. \quad (4)$$

This function peaks at rigidity

$$P_{\max,s} = \left(\frac{\alpha k}{k+1} \right)^{1/k}, \quad (5)$$

which for $\alpha = 9.5$, and $k = 0.93$ at sea level has a value of $P_{\max,s} = 5.1$ GV. For large values of P the differential counting rate becomes a power law of the form $-dN/dP = \alpha k N_0 P^{-k-1}$. Its maximum value is

$$-(dN/dP)_{\max} = N_0 [(k+1)/e]^{1+1/k} (\alpha k)^{-1/k}. \quad (6)$$

The median rigidity is defined as that value below and above which half the counts of the instrument are contributed. It is given by

$$P_{\text{median}} = \left[-\frac{1}{\alpha} \ln \left\{ \frac{1 + \exp(-\alpha P_c^{-k})}{2} \right\} \right]^{-1/k}. \quad (7)$$

For $P_c = 0$, i.e. for polar neutron monitors, this reduces to $P_{\text{median}} \approx (\alpha/\ln 2)^{1/k}$, which has a value of ≈ 14 GV. On the other hand, for equatorial neutron monitors with $P_c = 15$ GV, $P_{\text{median}} \approx 40$ GV.

[13] The name differential response function is reserved for the quantity

$$-\frac{d \ln N}{dP} = -\frac{1}{N} \frac{dN}{dP} = \frac{\alpha k P^{-k-1}}{\exp(\alpha P^{-k}) - 1}, \quad (8)$$

i.e. the fractional change in counting rate with rigidity. If P is large, this also becomes a power law of the form $-d \ln N/dP = k/P$. This function peaks at a rigidity $P_{\max,r}$ such that $\exp(-\alpha P_{\max,r}^{-k}) = 1 - [\alpha k / (k+1)] P_{\max,r}^{-k}$. For the nominal values $\alpha = 9.5$ and $k = 0.93$ at sea level, this value is $P_{\max,r} = 6.4$ GV, i.e. somewhat higher than $P_{\max,s} = 5.1$ GV. At this peak rigidity

$$-(d \ln N/dP)_{\max} = \left(k+1 - \alpha k P_{\max,r}^{-k} \right) / P_{\max,r} \quad (9)$$

has a value of only 5.6% per GV, which means that the response function is quite wide.

[14] The first three lines of Table 2 show the values of α , k , $P_{\max,s}$, $-(1/N_0)(dN/dP)_{\max}$, $P_{\max,r}$, $-(d \ln N/dP)_{\max}$, and P_{med} for the nominal values of α and k , and for the 1976 $qA > 0$ and 1987 $qA < 0$ solar minimum surveys at sea level. Figure 3 is a plot of the normalized neutron monitor differential counting rate $-(1/N_0)(dN/dP)$ in (4) and the differential response function (8), to demonstrate the difference between them. The nominal values of $\alpha = 9.5$ and $k = 0.93$ are used. These two sea-level differential response functions are also shown in Figure 6.

4. Kinetic Energy and Rigidity Spectra

[15] The spectra in Figure 1 are rigidity (P) spectra, converted from spectra as function of kinetic energy per nucleon, T . For the purpose of calculating atmospheric yield functions it is important to understand this conversion in detail. We therefore write it out in full.

[16] Particle “energy” is usually expressed in terms of momentum p , rigidity P , speed $\beta = v/c$, or kinetic energy per

Table 3. Relative Abundance in Percent of Cosmic-Ray Species at Relativistic Energies (10.6 GeV/nucleon)^a

	Nuclei per Unit K.E./Nucleon	Nucleons per Unit K.E./Nucleon	Nuclei per Unit Rigidity
H	94.8	76.9	84.9
He	4.6	14.9	13.3
CNO	0.4	4.6	1.1
Other	0.2	3.6	0.7

^aThe numbers in the first column are from *Gaisser and Stanev* [2010]. The “Other” species consist of Li, Be, B and the $Z > 8$ nuclei.

nucleon (instead of per nucleus), T . The relationship between these four variables is

$$P = pc/q = A/Z\sqrt{T(T + 2E_0)} = (A/Z)\beta(T + E_0) \quad (10)$$

where A and Z are mass and charge number respectively, and $E_0 = 938$ MeV is the proton rest mass energy.

[17] Let $j_T(T)$ denote the intensity spectrum of a species in particles per unit area, unit time, unit solid angle and unit kinetic energy per nucleon. This categorization is denoted by the subscript T . The second T in brackets is necessary to express explicitly that this spectrum is plotted as a function of kinetic energy per nucleon. Let this spectrum be any unspecified function of T , i.e. $j_T(T) = f(T)$. This means that the kinetic energy per nucleon spectrum as function of rigidity is given by $j_T(P) = f\left[\sqrt{Z^2P^2/A^2 + E_0^2} - E_0\right]$. Furthermore, a given number of particles, counted in terms of kinetic energy per nucleon must be the same as when counted in terms of rigidity. This requires that $j_P(P)dP = j_T(T)dT$. Using dT/dP from (10), one finds that the ratio of a rigidity spectrum for a species s relative to the spectrum for H is

$$\frac{j_P(P)_s}{j_P(P)_H} = \frac{Z^2}{A^2} \frac{\sqrt{P^2 + E_0^2}}{\sqrt{Z^2P^2/A^2 + E_0^2}} \frac{f\left[\sqrt{Z^2P^2/A^2 + E_0^2} - E_0\right]}{f\left[\sqrt{P^2 + E_0^2} - E_0\right]}. \quad (11)$$

The relativistic limit, when $ZP/A \gg E_0$, is

$$\frac{j_P(P)_s}{j_P(P)_H} = \frac{Z}{A} \frac{f(ZP/A)}{f(P)}, \quad (12)$$

while the non-relativistic limit, when $ZP/A \ll E_0$, is

$$\frac{j_P(P)_s}{j_P(P)_H} = \left[\frac{Z}{A}\right]^2 \frac{f\left[0.5(ZP/A)^2\right]}{f(0.5P^2)}. \quad (13)$$

Gaisser and Stanev [2010] show kinetic energy spectra of 11 different primary species as function of kinetic energy per nucleus (i.e. total kinetic energy). When the scale is converted to kinetic energy per nucleon, to first order these spectra all have the same form. Above a few GeV per nucleon they are simple power laws of the form $f(T) = T^{-\gamma}$. In this case the relativistic and non-relativistic ratios reduce to $(Z/A)^{1-\gamma}$ and $(Z/A)^{2-\gamma}$, respectively. For the value of $\gamma = 2.7$ derived from Figure 1, the relativistic and non-relativistic ratios are 3.25 and 1.62, respectively. This means that the abundance of species s relative to H on a rigidity scale is boosted by these two numbers relative to the ratio on a kinetic energy per nucleon scale.

[18] It is noteworthy that a rigidity-discriminating detector such as a neutron monitor inside the atmosphere has quite a high response to the heavier cosmic-ray species. The first column of Table 3 is taken from *Gaisser and Stanev* [2010], and it contains the relative abundance of cosmic-ray species when they are categorized in the usual way, in terms of particles (or nuclei) per unit kinetic energy per nucleon. The atmospheric production process and consequent detector response, however, are almost independent of whether these nuclei are individual protons (H) or whether they are bound in nuclei. Consequently, a more important quantity is the number of nucleons per unit kinetic energy per nucleon as shown in the second column. However, these individual nucleons from the heavier species each have only half the kinetic energy of the nucleon that originated from a primary proton. Therefore, they are only half as effective to produce further cascades. To circumvent this problem, we show in the next paragraph how the rigidity spectra in the third column of Table 3 should be used to determine the atmospheric yield function.

5. Calculated Yield Functions

[19] The production of secondary particles that leads to the counting rate described by (1) is simulated by several widely used Monte Carlo programs mentioned in the Introduction. One of these is the FLUKA program. *Clem* [1999] wrote ancillary routines to this general code to simulate the NM64 and IGY neutron monitor response for these secondary particles, i.e. to calculate the neutron monitor yield function $S(P, x)$. Many of their results are reported in *Clem and Dorman* [2000]. Figure 4, reproduced from their Figure 10a, shows the calculated yield functions for vertically incident

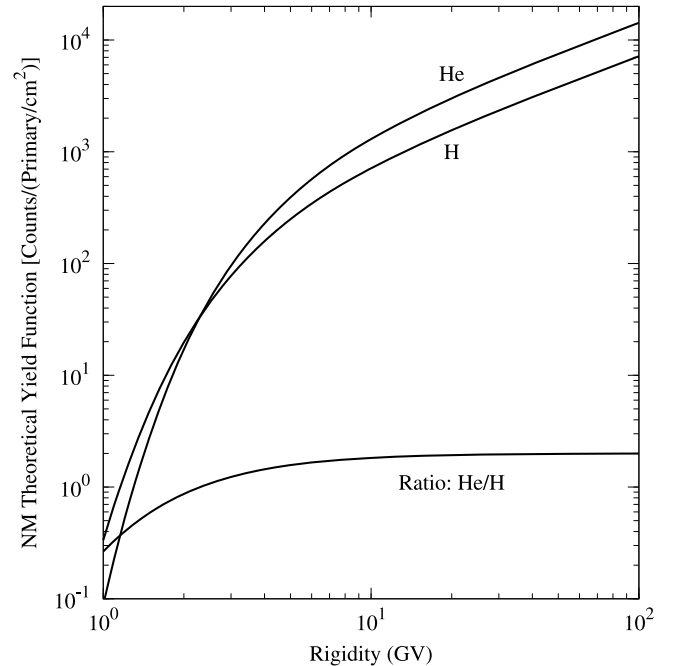


Figure 4. Calculated neutron monitor yield functions at sea level from *Clem and Dorman* [2000]. The curves are double power laws of the form (2), with coefficients given in the lines CD00 and He/H yield in Table 1.

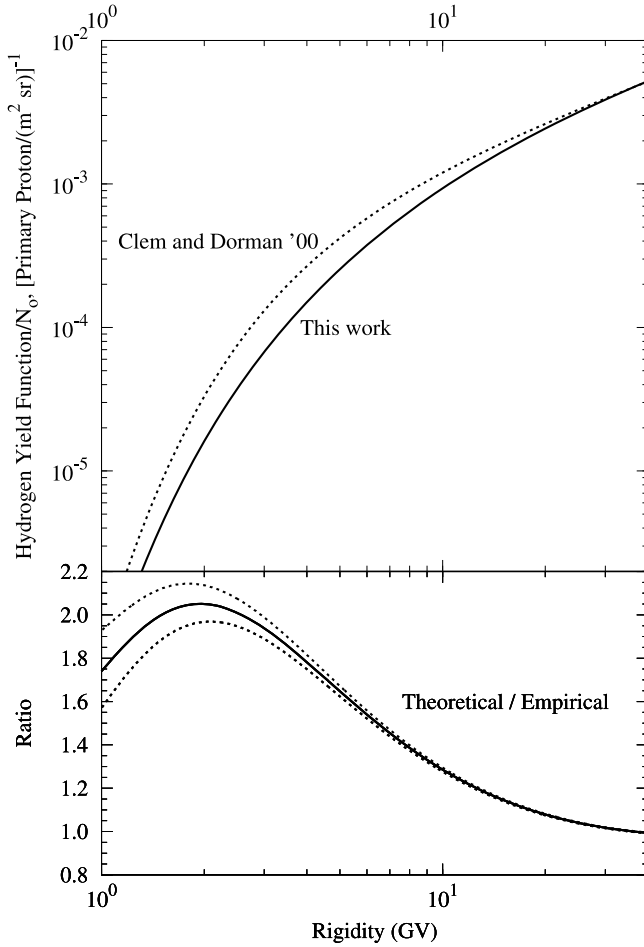


Figure 5. Empirical (this work) and theoretical normalized specific H yield functions at sea level. Parameters are shown in the lines “This work” and “CD00” in Table 1. The reduced chi-squared value for the former is 1.2. In the bottom panel the uncertainty band is due to an uncertainty of $\pm 1\%$ in the counting rate of a neutron monitor at 5 GV. Note that above 15 GV the empirical yield function is based on a pure extrapolation of the Dorman function.

H and He nuclei for an NM64 neutron monitor at sea level (atmospheric pressure $x_{sl} = 760$ mm Hg, atmospheric depth $= 1033$ g/cm²).

[20] At relativistic rigidities the yield is proportional to P , while the ratio of the He to H yield is a factor of 2. This simple scaling can be understood from the fact that for a given rigidity P , the ratio of the kinetic energy of a nucleus with A and $Z > 1$ relative to that of a proton is

$$\frac{T_{\text{nucleus}}}{T_{\text{H}}} = Z \left[\frac{\sqrt{P^2 + (A/Z)^2 E_0^2} - (A/Z)E_0}{\sqrt{P^2 + E_0^2} - E_0} \right] \quad (14)$$

The relativistic and non-relativistic limits are Z and $Z/2$ respectively, while at $P = 1$ GV the ratio is $0.57Z$. Hence, for a given rigidity, the yield functions for these two species should be in the same proportion. For He these ratios are $S_{\text{He}}/S_{\text{H}} = 2$ for $P \gg 1$ GV, $S_{\text{He}}/S_{\text{H}} = 1.14$ for $P = 1$ GV, and $S_{\text{He}}/S_{\text{H}} = 1$ for $P \ll 1$ GV. Figure 4 shows, however, that

toward the lower rigidities, the ratio becomes much smaller. This is due to a second effect. The particle speed as function of rigidity is $\beta = P/\sqrt{P^2 + (A/Z)E_0^2}$. Thus, at non-relativistic rigidities the primary He nucleus has only half the speed of the proton, and it loses energy due to ionization much faster, leaving less remaining energy to produce further secondary nucleons.

[21] These two combined effects can be described by the double power-law function $S_{\text{He}}/S_{\text{H}} = F(P)$ as in (2), with the coefficients in the last line of Table 1.

6. Empirical Yield Functions

[22] Figure 5 shows the empirical yield function as derived from the differential counting rate at sea level, $-dN/dP$, from the 1987 latitude survey in Figure 2 with the parameters as in the third line of Table 2.

[23] This yield function is derived by inverting the integrand of (1):

$$-dN/dP = S_{\text{H}}j_{\text{H}}(P) + S_{\text{He}}j_{\text{He}}(P) + S_{\text{CNO}}j_{\text{CNO}}(P) + S_{\text{other}}j_{\text{other}}(P) \quad (15)$$

to obtain the proton yield function, S_{H} , as follows:

$$S_{\text{H}} = \frac{-(dN/dP)}{j_{\text{H}}(P) + \left(\frac{S_{\text{He}}}{S_{\text{H}}}\right)j_{\text{He}}(P) + \left(\frac{S_{\text{CNO}}}{S_{\text{H}}}\right)j_{\text{CNO}}(P) + \left(\frac{S_{\text{other}}}{S_{\text{H}}}\right)j_{\text{other}}(P)} \quad (16)$$

In the previous section we found that $S_{\text{He}} = F(P)S_{\text{H}}$. The relationship between the yield functions for the heavier species is simpler, because they all have $A/Z = 2$. Using (14) it follows that the ratio of total energies is $T_{\text{nucleus}}/T_{\text{He}} = Z_{\text{nucleus}}/Z_{\text{He}} = Z_{\text{nucleus}}/2$, for all rigidities. Hence $S_{\text{nucleus}} = (1/2)Z_{\text{nucleus}}F(P)S_{\text{H}}$. Since all species with $A/Z = 2$ have the same speed for a given rigidity, there is no further factor $F(P)$ involved.

[24] Putting these relations into (16) gives

$$S_{\text{H}} = \frac{-(dN/dP)}{j_{\text{H}}(P) + F(P)j_{\text{He}}(P)[1 + 3.5j_{\text{CNO}}/j_{\text{He}} + 5.6j_{\text{other}}/j_{\text{He}}]} \quad (17)$$

Using the numbers in the third column of Table 3 we therefore arrive at

$$S_{\text{H}} = \frac{-(dN/dP)}{j_{\text{H}}(P) + 1.584F(P)j_{\text{He}}(P)}. \quad (18)$$

This expression reveals that a neutron monitor has a large sensitivity to species heavier than H: At rigidities ≥ 6 GV, just above maximum neutron monitor response is, $F(P) \approx 2$. Then, putting in the values for $j_{\text{H}}(P)$ and $j_{\text{He}}(P)$ from the last column of Table 3 into (17), gives $S_{\text{H}} = -(dN/dP)/(1.496j_{\text{H}})$. This means that for a neutron monitor at sea level only $1/1.496 = 67\%$ of the counts are due to protons, while 33% are due to heavier species.

[25] This proton yield function is shown in Figure 5, together with the theoretical proton yield function of Figure 4, as well as the ratio of the two. In order to compare these yield functions, in Figure 5 we multiplied the theoretical proton yield function by 0.017, which gives a ratio of 1

Table 4. Counting Rates N_0 at Sea Level and at Cutoff Rigidity <1 GV for Different Cosmic-Ray Detectors

CR Detector	N_0 (counts/hour)
3NM64	125000
1NM64	31250
12IGY	25000
Strat. Det.	1200
GRAND MT	4.96×10^6

above 40 GV where both yield functions are $\propto P^{0.89}$. This shows that in the region of a few GV, where the response function is high, the theoretically calculated value is up to twice as large as the empirically derived value, while at higher rigidities the calculated value is too low. The normalization in Figure 5 is such that the units of S/N_0 are $[\text{primary protons}/\text{m}^2/\text{sr}]^{-1}$. One has to multiply with N_0 to get the number of counts per primary proton per m^2 per sr. This number is given for several typical detectors in Table 4. The dashed lines in the bottom part are due to the experimental uncertainties described in section 2. This implies that the difference between calculated and empirical atmospheric yield functions is now significantly larger than the experimental uncertainties. However, in Figure 5 we compared the calculated (theoretical) yield function for vertically incident H with the empirical yield function for omni-directionally incident H.

7. Altitude, Detector and Solar Cycle Dependence

[26] Having compared the empirical and theoretical neutron monitor yield functions at sea level during the solar minimum of 1987, we now extend them to other periods and altitudes and also to different detectors.

[27] The counting rate of a neutron monitor inside the atmosphere varies with depth x as $d \ln N = -\beta dx$, where β is called the barometric, pressure or attenuation coefficient. (Notice that this β is not the same as $\beta = v/c$ used previously.) It has a value of approximately 0.74% per g/cm^2 , or 1% per mm Hg. Consequently, the parameterized counting rate of a neutron monitor can be written as

$$N(P_c, x, t) = N_0 [1 - \exp(-\alpha P_c^{-k})] \exp[\beta(x, P_c, t)(x_{sl} - x)], \quad (19)$$

where the normalization is such that N_0 is the counting rate of a polar neutron monitor ($P_c < 1$ GV) at sea level (sl). We have explicitly noted that the pressure coefficient depends on atmospheric pressure (or depth), x , cutoff rigidity P_c , and time t during the modulation epoch. *Raubenheimer and Stoker* [1974, and references therein] have studied this x, P_c, t dependence. They show that at $P_c = 15$ GV, β ranges from 0.56 to 0.70%/(g/cm^2) from sea level to 30 000 ft, and from 0.70 to 0.78%/(g/cm^2) at 1 GV. The variation with solar activity is considerably smaller than this altitude variation.

[28] There is, however, an alternative way to parameterize the altitude dependence, by writing:

$$N(P_c, x, t) = N_0 [1 - \exp(-\alpha(x)P_c^{-k(x)})] \exp[\beta(x_{sl} - x)], \quad (20)$$

and where α and k are taken as linear functions of atmospheric pressure (x):

$$\begin{aligned} \alpha(x) &= \alpha_{sl} + m_\alpha(x_{sl} - x) \\ k(x) &= k_{sl} + m_k(x_{sl} - x), \end{aligned} \quad (21)$$

and where β is a constant, independent of x, P , and t . This alternative parameterization is useful because in 1976 two latitude surveys were conducted: the one at sea level and a second one at 30 000 ft altitude (atmospheric depth $x = 307 \text{ g}/\text{cm}^2$), measured by *Stoker and Moraal* [1995]. It is simpler to measure the counting rates at two different altitudes and calculate the altitude dependence from this, than to measure the altitude dependence at several cutoff rigidities and calculate the counting rates at these altitudes. Only a linear interpolation is used because there are only measurements at two altitudes.

[29] The top curve of Figure 6 shows this differential response function, which results from a fit of the “76” data of the middle curve of Figure 3 of *Stoker and Moraal* [1995]. The parameters α and k for this fit are shown in the fourth line of Table 2.

[30] From these two neutron monitor differential response functions in 1976, it follows from (21) that $m_\alpha = -0.0013 \text{ (g}/\text{cm}^2)^{-1}$, $m_k = 0.00041 \text{ (g}/\text{cm}^2)^{-1}$, and $\beta = 0.00710 \text{ (g}/\text{cm}^2)^{-1}$.

[31] Figure 6 also shows a differential response function at 30 000 ft (9144 m) for the $qA < 0$ solar minimum in 1987.

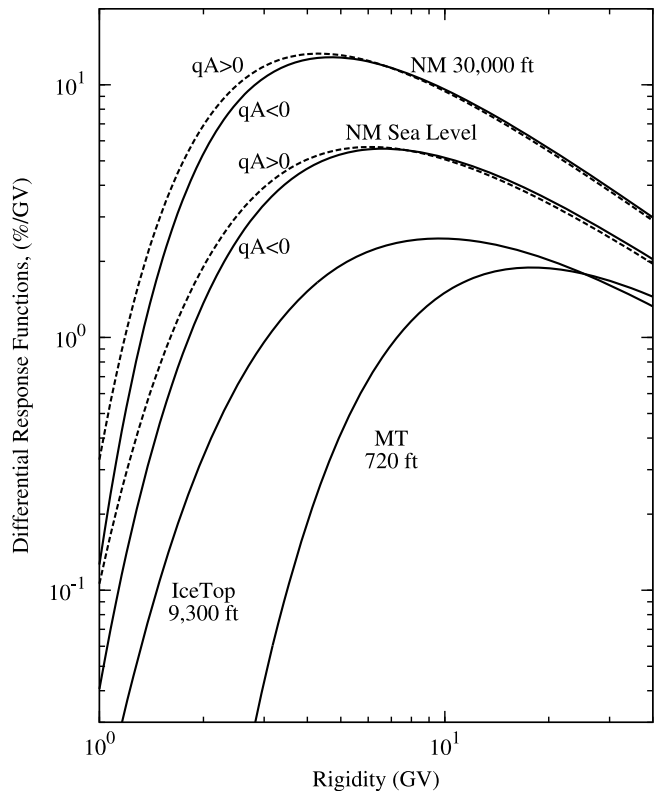


Figure 6. Neutron monitor differential response functions, $-d \ln N/dP$, at sea level and at 30,000 ft, calculated from (8) and the parameters in Table 2. The GRAND muon telescope response function is at 720 ft and the IceTop detector at 9,300 ft.

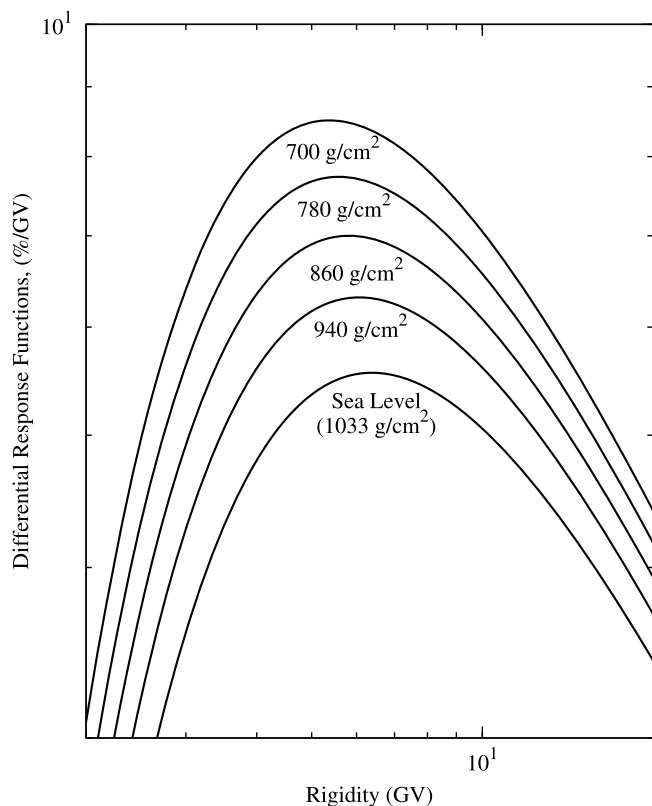


Figure 7. Neutron monitor differential response functions for different atmospheric depths. The nominal values of $\alpha = 9.50$ and $k = 0.93$ in the first line of Table 2 were used.

This response is not explicitly measured. It is rather derived from the empirically derived sea level response, and by assuming that the altitude dependence is the same as for 1976, i.e. using the values of m_α , m_k and β above.

[32] Figure 7 shows a series of neutron monitor differential response functions in the altitude range in which most neutron monitors occur. They were calculated from the empirical sea level curve, once again using the coefficients m_α , m_k and β as calculated above.

[33] Figure 6 also contains a response function for the GRAND muon telescope at 1005 g/cm^2 (220 m), using the parameters in the last line of Table 2. The yield function used for this response function was read off from the dashed line in Figure 3 of *Poirier and D'Andrea* [2002]. It was calculated by them using the FLUKA code. In comparison with neutron monitors, this response function is much harder, with hardly any response below 3 GV. The parameters in Table 2 show that the maximum response is only 2.6% per GV at 18 GV, versus 5.5% per GV at ≈ 6 GV for a neutron monitor at sea level. Similarly, Figure 6 also contains the differential response function for the IceTop Cherenkov detector, calculated from the yield function obtained by *Clem et al.* [2008], which responds to even higher rigidities. It should be noted that the accuracy of these calculation have not been tested experimentally with latitude surveys as was done for neutron monitors.

[34] Next, we focus on a series of remarkable stratospheric balloon experiments conducted over the last more than 50 years by scientists of the Lebedev Institute in Moscow,

described by *Stozhkov et al.* [2009]. These daily flights routinely reach atmospheric depths as low as 5 g/cm^2 , and hence the spectra of these measurements should be much softer than those of neutron monitors. *Moraal and Stoker* [2010] showed how useful these measurements at lower effective rigidities are to characterize the rigidity dependence of the unusually high cosmic-ray maximum during the 2009 solar minimum period. This, and another similar modulation calculations, require a quantitative comparison of the balloon response functions with those of neutron monitors. Figure 8 shows three such differential response functions for this balloon detector, at 300, 100 and 40 g/cm^2 . These response functions are “Dorman fits” (3) to the counting rates as function of atmospheric pressure in Figure 6 of *Stozhkov et al.* [2009], (with the data points supplied by Y. Stozhkov). The parameters of the fit are given in the three relevant lines of Table 2. The rigidities of maximum response and the mean rigidities are considerably lower than those of neutron monitors, indicating much softer spectra. For instance, at 40 g/cm^2 the peak response is only at 2.9 GV, and it has a maximum value of $\sim 15\%/GV$ in comparison of $6\%/GV$ at ~ 6 GV for a neutron monitor at sea level. On the other hand, for a given atmospheric pressure, the stratospheric balloon has a much lower response than the neutron monitor. This is shown by the 1987 neutron monitor differential response function at sea level from Figure 6, which is repeated here in Figure 8. It shows that the

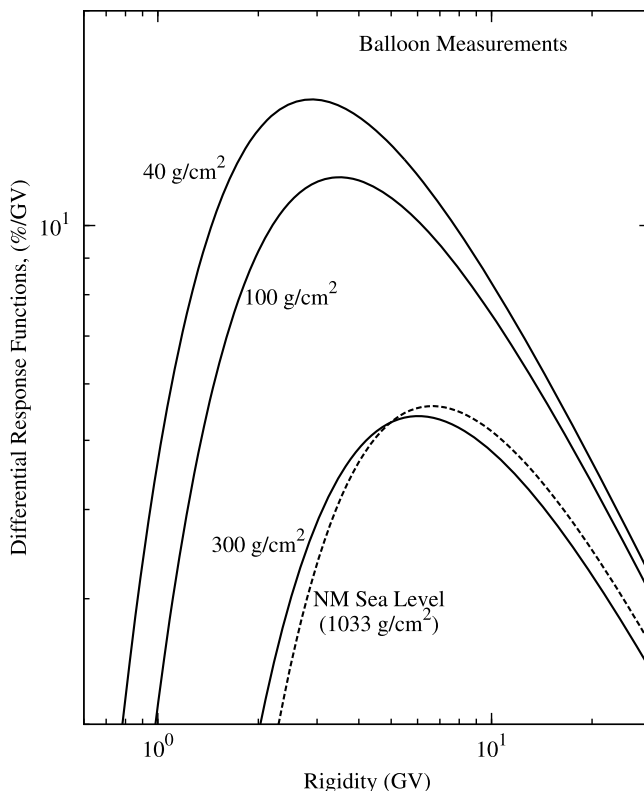


Figure 8. Stratospheric balloon differential response functions, $-d\ln N/dP$, at three altitudes in the atmosphere, calculated from (8) and the parameters in Table 2. The neutron monitor differential response function at sea level is also shown for comparison.

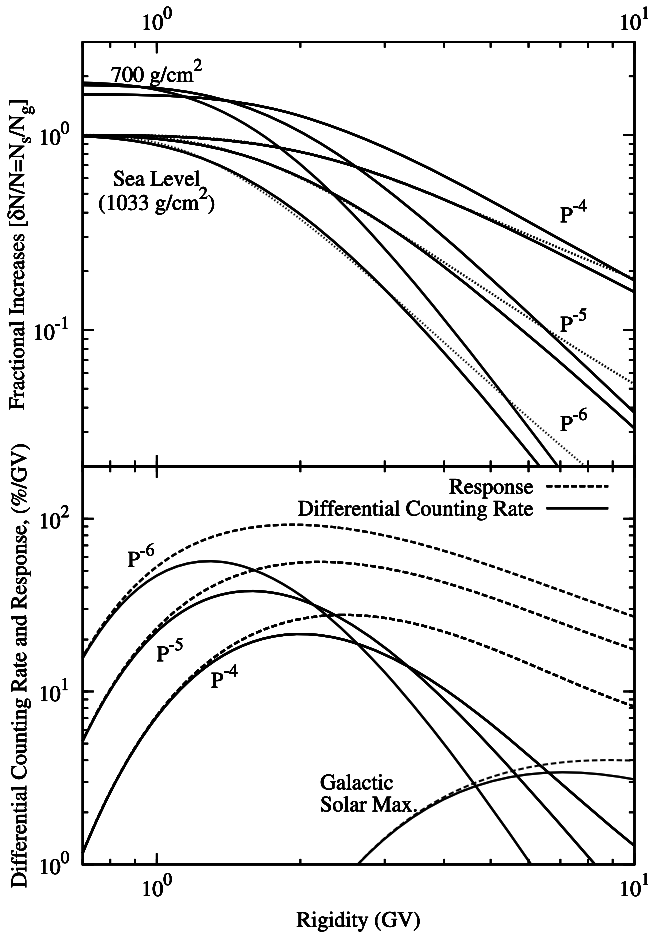


Figure 9. (top) Neutron monitor fractional increases $\delta N/N$ at sea level and 700 g/cm^2 for solar proton events. (bottom) Response functions and differential counting rates. Dotted lines in the top panel show the fit to sea-level counts with the Dorman function (3) and the parameters in the last three lines of Table 2. For comparison, the neutron monitor response and differential counting rate for galactic cosmic rays at solar maximum are shown in the bottom panel.

stratospheric detector at 300 g/cm^2 ($\approx 30\,000 \text{ ft}$) has almost the same response as the neutron monitor at sea level.

[35] For this balloon experiment, it follows from (21) that $m_\alpha = -0.0155 \text{ (g/cm}^2\text{)}^{-1}$, $m_k = 0.00057 \text{ (g/cm}^2\text{)}^{-1}$, and $\beta = 0.00318 \text{ (g/cm}^2\text{)}^{-1}$. When these parameters are used, one can make a rough estimate of the stratospheric detector's response at sea level. This is shown in the fourth line of the detector's response in Table 2. This extrapolation is evidently very inaccurate, but the very large maximum and median rigidities indicate that there is almost no response so deep inside the atmosphere.

[36] The above response functions are for typical solar minimum conditions. The solar cycle dependence can be calculated to first order by using the Force-Field approach as described in *Caballero-Lopez and Moraal* [2004]. The lowest counting rates ever recorded were in June 1991, when the Sanae ($P_c = 0.8 \text{ GV}$), Hermanus ($P_c = 4.9 \text{ GV}$), and Tsumeb ($P_c = 9.1 \text{ GV}$) neutron monitor counting rates had decreased to 74%, 78%, and 84% of the solar minimum

values of March 1987, respectively. From (18) it follows that these counting rates can be expressed as

$$N_{\text{solar max}} = \int_{P_c}^{\infty} S_H(P) [j_{\text{H,solar max}}(P) + 1.584F(P)j_{\text{He,solar max}}(P)] dP. \quad (22)$$

The solar minimum spectra are those in Figure 1. The Force-Field formalism requires that $j_{\text{solar max}} = (P_{\text{solar max}}/P_{\text{solar min}})^2 j_{\text{solar min}}$, and the relationship between $P_{\text{solar max}}$ and $P_{\text{solar min}}$ is given by:

$$\Delta\phi = \sqrt{P_{\text{solar min}}^2 + (AE_0/Z)^2} - \sqrt{P_{\text{solar max}}^2 + (AE_0/Z)^2}. \quad (23)$$

As explained in *Caballero-Lopez and Moraal* [2004], $P_{\text{solar max}}$ and $P_{\text{solar min}}$ are such that if particles had rigidity P in the unmodulated spectrum, then $(P - P_{\text{solar max}})$ and $(P - P_{\text{solar min}})$ represent the Force-Field rigidity loss under solar maximum and solar minimum conditions, respectively. The Force-Field parameter is $\phi = (\beta\kappa_2/3)M$, with M being the modulation integral $M = \int (Vdr/\kappa)$, integrated from Earth to the outer boundary of the heliosphere, where the diffusion coefficient is separable in the form $\kappa = \beta\kappa_1(r)\kappa_2(P)$, and where it is assumed that $\kappa_2 = P$ in units of GV. It is then found by iteration that the correct values of $N_{\text{solar max}}$ are correctly reproduced if $\Delta\phi = 0.95 \text{ GV}$. Finally, the Dorman fit (3) is done for $N_{\text{solar max}}$, with the parameters given in the line Nominal SL (solar max.) of Table 2.

8. Ground-Level Enhancements

[37] The calculations above are all for galactic cosmic rays (GCRs). However, solar eruptions in the form of coronal mass ejections and flares occasionally produce so-called ground-level enhancements (GLEs) in the counting rate of neutron monitors. On average they occur only once per year, because they represent the highest energies in solar energetic particle spectra, and the acceleration mechanisms on the Sun are only occasionally strong enough to accelerate the particles to rigidities $P > 1 \text{ GV}$ (proton energy $> 400 \text{ MeV}$), so that they can be detected by ground-based neutron monitors. These outward-propagating particles are not modulated as for GCRs, so that when the particles arrive at Earth, the GLE spectra are still approximately power laws of the form $j \propto P^{-\gamma}$, with typical values of γ ranging from 4 to 6. Since the spectra are softer than for GCRs, the rigidity of maximum response and the median rigidity are much lower, and the altitude effect is much larger.

[38] The beginning phases of GLEs are usually highly anisotropic, and it is difficult to separate spectral from anisotropic effects. The following analysis is only valid for the isotropic part. These parameterized results are useful to separate the isotropic and anisotropic parts of the increases.

[39] For GLEs the solar contribution, N_s , to the counting rate is always superimposed on the galactic cosmic-ray background, N_g , so that the observable quantity is the fractional increase $\delta N/N = N_s/N_g$.

[40] Figure 9 (top) shows these fractional increases in neutron monitor counting rates as function of cutoff rigidity for power-law input spectra with indices of -4 , -5 and -6 . The bottom three curves are for sea level (1033 g/cm^2), and

the top three for atmospheric depth of 700 g/cm². This atmospheric depth is representative for the neutron monitor at South Pole at altitude of 2835 m, which makes it the most sensitive neutron monitor to detect such GLEs. Figure 9 (bottom) shows the corresponding sea-level differential response functions $d\ln(\delta N/N)/dP = d\ln N_s/dP - d\ln N_g/dP$, and the differential counting rates of the increases, $d(\delta N/N)/dP = (N_g/N_s)d\ln(\delta N/N)/dP$. The differential counting rate and response function for GCR at solar maximum conditions are shown for comparison.

[41] Figure 9 (top) also shows that the sensitivity of neutron monitors to these steep spectra diminishes fast with increasing cutoff rigidity. So, for instance, for a P^{-4} spectrum, a neutron monitor at sea level and $P_c = 5$ GV will record a GLE increase of only 36% of that of a polar neutron monitor at $P_c < 1$ GV. For P^{-5} and P^{-6} this fraction is only 14% and 4%. This explains why the Hermanus neutron monitor at $P_c = 4.9$ GV, for instance, has only seen one large GLE since 1957, namely an increase of $\sim 100\%$ during the GLE of 29 September 1989.

[42] The counting rate N_g at sea level was calculated from the Dorman function (3) with the coefficients α and k given in the line ‘‘Nominal SL (solar max.)’’ in Table 2. The solar maximum value was used because GLEs tend to occur toward solar maximum. At 700 g/cm² the same fitting function was used but with the coefficients $\alpha = 12.36$ and $k = 1.08$, calculated from the altitude dependence in (21). This produces a counting rate at 700 g/cm² (at $P_c < 1$ GV) that is ≈ 13 times higher than at sea level. The counting rates due to solar particles were calculated from

$$N_s(P_c, x) = \int_{P_c}^{\infty} S_H(P_c, x) j(P) dP, \quad (24)$$

where S_H at sea level is a double power-law function given by (2) with coefficients in the line ‘‘This work’’ in Table 1, and S_H at $x = 700$ g/cm² is from (18), using dN/dP in (4) with coefficients $\alpha = 12.36$ and $k = 1.08$ as above. The power-law spectrum $j(P) \propto P^{-\gamma}$ was normalized so that N_s at sea level and at $P_c < 1$ GV is equal to 1. This produces a counting rate at 700 g/cm² (at $P_c < 1$ GV) that is between 20 and 24 times higher than at sea level, depending on the steepness of the power-law spectrum. Consequently, the fractional increases are between 1.55 (20/13) to 1.85 (24/13) times larger at 700 g/cm² than at sea level. This agrees with observations from the data base of *Moraal and McCracken* [2011] that GLE increases on the South Pole neutron monitor are typically 1.5 to 2 times larger than at sea level.

[43] The altitude effect can be expressed in terms of an effective attenuation coefficient that was introduced by *McCracken* [1962] as follows. From the definition $\beta_s = (\delta x)^{-1} \ln[N_s(x)/N_{s0}(x)]$ it follows that at 2 GV $\beta_s = 0.00877$ (g/cm²)⁻¹ for a solar spectrum $\sim P^{-6}$, in comparison with the GCR value $\beta_g = 0.00710$ (g/cm²)⁻¹ found in the previous section. Since $N_g = N_{g0} \exp(\beta_g \delta x)$ and $N_s = N_{s0} \exp(\beta_s \delta x)$, it follows that

$$\frac{\delta N}{N} = \frac{\delta N_0}{N_0} e^{\beta \delta x}, \quad (25)$$

where $\beta = \beta_s - \beta_g = 0.00877 - 0.00710 = 0.00167$ (g/cm²)⁻¹. This is the equivalent of the two path-length formalism of *McCracken* [1962], who used the absorption path-length $\lambda \equiv 1/\beta$, to find $\lambda_g = 141$ g/cm², $\lambda_s = 114$ g/cm² and $\lambda = 596$ g/cm². When converted, our values are $\lambda_g = 138$ g/cm², $\lambda_s = 111$ g/cm² and $\lambda = 584$ g/cm².

[44] A Dorman fit was done to the three sets of counting rates N_s at sea level, and the parameters are shown in the last three lines of Table 2. When these fits are used instead of the true values, it results in the dotted lines for the sea-level fractional increases in Figure 9 (top). These fits are not as good as for GCRs. The reason is that the spectra are now much steeper, and a single α and k are insufficient for a good fit. Hence the coefficients were chosen to give the best fits at low rigidities (≈ 2 GV) where the response is largest. The magnitude of the deviation is overemphasized by the logarithmic scale. For instance, for the P^{-5} spectrum the true increase at 10 GV is 3% of that at 1 GV, while the Dorman fit gives 5%. This difference is smaller than other uncertainties associated with very infrequent GLEs at such high rigidities. Hence we regard the fits in the last three lines of Table 2 as adequate. Because the GCR contribution at low rigidities is so small, the parameters for $(\delta N/N)$ are very similar to those of N_s in the last three lines of Table 2. This quantifies the softness of the spectra in the bottom part of Figure 9, and it shows that the maximum GLE response is in the range $1.6 < P_c < 2.6$ GV, in comparison with ≈ 6 GV for GCRs. Similarly, the median rigidity for polar stations at $P_c < 1$ GV is $1.8 < P_{\text{med}} < 3.7$ GV, compared to ≈ 16 GV for GCRs.

[45] Finally, we note that at 10 GV the fractional increases $\delta N/N$ at 700 g/cm² are only ≈ 1.2 times larger than at sea level, while at < 1 GV it is 1.55 to 1.85 times. This is due to a rigidity dependence in β_s , which ranges from 0.00894 (g/cm²)⁻¹ at 1 GV, to 0.00718 (g/cm²)⁻¹ at 10 GV. This is a small, secondary effect because few GLEs are observed at such high rigidities, but in a subsequent paper we will show how it can be used as a diagnostic to infer GLE spectral shapes.

9. Summary

[46] The purpose of this paper was to find a simple and useful parameterization of neutron monitor yield and response functions in the atmosphere. These results are ever more widely used in applications such as radiation dose calculations and the influence of cosmic rays on atmospheric processes. The main results are compiled in Table 2 and the noteworthy points are:

[47] 1. During solar minimum conditions the primary spectra of H and He above the atmosphere can be conveniently expressed by a double power-law function given in (2), with the coefficients given in the first two lines of Table 1. It is important for double power-law fits not to use them outside their range of validity.

[48] 2. Neutron monitor counting rates, as well as those of other detectors inside the atmosphere, can be conveniently expressed in terms of the well-known Dorman function (3). This function is analytically differentiable, so that it gives analytical expressions for the differential counting rate, $-dN/dP$, and the differential response function, $-d\ln N/dP$,

for a given detector in the atmosphere, cf. expressions (4) and (8). The rigidities where these functions peak, and the peak values are also readily calculated as in (5), (6), (7) and (9). The parameters for these functions are shown in Table 2 for neutron monitors, the Russian stratospheric balloon detector, the GRAND muon telescope, and the IceTop Cherenkov detector. The differential response functions are plotted in Figures 3, 6, 7, and 8.

[49] 3. The differential counting rate, $-dN/dP$, and the counting rate N of a neutron monitor as given by (1) are calculated at a given time from (18), where S_H and $F(P)$ are given in the line “This work” and the last line of Table 1, and where j_H and j_{He} are the measured primary spectra at that time.

[50] 4. The yield function study shows that only about 67% of the counts of a neutron monitor are due to protons, with the rest from heavier species.

[51] 5. It is noteworthy from Figure 8 that the response of the stratospheric detector at 30 000 ft altitude (307 g/cm^2) is almost the same as that of the neutron monitor at sea level (1033 g/cm^2); and the response at 100 g/cm^2 is similar to that of a neutron monitor at 307 g/cm^2 . As far as we are aware, this is the first quantitative comparison between these two classes of detector. It shows that the stratospheric detector has a much weaker response, but its virtue is that it flies very high up in the atmosphere, at 40 g/cm^2 , where its peak response is about three times higher, and at about three times lower median rigidity, than for a neutron monitor at sea level. Hence, this detector measures a much stronger modulation signal than neutron monitors, and it fills an important role in modulation studies.

[52] 6. Figure 5 compares the yield function of protons calculated from numerical simulations of cascades in the atmosphere with the empirically derived function. The highly accurate Pamela spectra that were used for the empirical yield function indicate that there is a significant difference between the two, which calls for further refinement of the cascade calculations.

[53] 7. The parameters of the double power-law fit to the yield function are shown in Table 1. They are shown for neutron monitors at sea level, and for the GRAND muon telescope and IceTop detectors. This double power-law fit is simpler than the parameterization of e.g. *Nagashima et al.* [1989].

[54] 8. The parameterization for GCRs was extended to typical power-law spectra observed during GLEs due to solar energetic particle events, and the relevant lines in Table 2 show that for a wide range of power-law input spectra, the maximum neutron monitor response stays between 1.6 and 2.6 GV. This only presents the first-order GLE effects. In a subsequent paper we refine this procedure by taking into account the spectral and rigidity dependence of β , to show for several events in solar cycle 23 how spectral information can be derived from the altitude dependence of the GLEs.

[55] **Acknowledgments.** This paper is dedicated to the memory of Frank B. McDonald of the University of Maryland who was host to both of us when part of this work was done. This work was supported by the South African National Research Foundation and a PASPA-UNAM grant.

References

- Adriani, O., et al. (2011), PAMELA measurements of cosmic-ray proton and helium spectra, *Science*, 33(6025), 69–72.
- Bazilevskaya, G. A., et al. (2008), Cosmic-ray induced ion production in the atmosphere, *Space Sci. Rev.*, 137, 149–173.
- Bieber, J. W., P. Evenson, J. E. Humble, and M. L. Duldig (1997), Cosmic-ray spectra deduced from neutron monitor surveys, *Proc. 25th ICRC*, 2, 45–48.
- Caballero-Lopez, R. A., and H. Moraal. (2004), Limitations of the force-field equation to describe cosmic-ray modulation, *J. Geophys. Res.*, 109, A01101, doi:10.1029/2003JA010098.
- Caballero-Lopez, R. A., H. Moraal, and F. B. McDonald (2004), Galactic cosmic-ray modulation: effects of the solar wind termination shock and the heliosheath, *J. Geophys. Res.*, 109, A05105, doi:10.1029/2003JA010358.
- Clem, J. M. (1999), Atmospheric yield functions and the response to secondary particles of the neutron monitors, *Proc. 26th ICRC*, 7, 317–320.
- Clem, J. M., and L. I. Dorman (2000), Neutron monitor response functions, *Space Sci. Rev.*, 93, 335–359.
- Clem, J. M., et al. (2008), Response of the IceTop tanks to low-energy particles, *Proc. 30th ICRC*, 1, 237–240.
- Dorman, L. I. (2009), *Cosmic Rays in Magnetospheres of the Earth and Other Planets*, *Astrophys. Space Sci. Library*, vol. 358, Springer Sci. and Business Media B.V., Dordrecht, Netherlands.
- Dorman, L. I., S. G. Fedchenko, L. V. Granitsky, and G. A. Rishe (1970), Coupling and barometer coefficients for measurements of cosmic-ray variations at altitudes of 260–400 mb, *Proc. 11th ICRC*, 2, 233–236.
- Dorman, L. I., G. Villorresi, N. Iucci, M. Parisi, M. I. Tyasto, O. A. Danilova, and N. G. Putsyna (2000), Cosmic-ray survey to Antarctica and coupling functions for neutron component near solar minimum (1996–1997): 3. Geomagnetic effects and coupling functions, *J. Geophys. Res.*, 105(A9), 21,047–21,056.
- Gaissner, T. K., and T. Stanev (2010), Cosmic rays, in *Review of Particle Physics*, *J. Phys. G*, vol. 37, edited by K. Nakamura et al., pp. 269–275, IOPscience Publ., Bristol, U. K.
- McCracken, K. G. (1962), The cosmic-ray flare effect: 1. Some new methods of analysis, *J. Geophys. Res.*, 67, 423–434.
- Moraal, H., and K. G. McCracken (2011), The ground-level enhancements of solar cycle 23, *Space Sci. Rev.*, 171, 85–95, doi:10.1007/s11214-011-9742-7.
- Moraal, H., and P. H. Stoker (2010), Long-term neutron monitor observations and the 2009 cosmic-ray maximum, *J. Geophys. Res.*, 115, A12109, doi:10.1029/2010JA015413.
- Moraal, H., M. S. Potgieter, and P. H. Stoker (1989), Neutron monitor latitude survey of cosmic-ray intensity during 1986/1987 solar minimum, *J. Geophys. Res.*, 94(A2), 1459–1464.
- Moskalenko, I. V., A. W. Strong, J. F. Ormes, and M. S. Potgieter (2002), Secondary antiprotons and propagation of cosmic rays in the galaxy and heliosphere, *Astrophys. J.*, 565, 280–296, doi:10.1086/324402.
- Nagashima, K., S. Sakakibara, K. Murakami, and I. Morishita (1989), Response and yield functions of neutron monitor, galactic cosmic-ray spectrum and its solar modulation, derived from all the available worldwide surveys, *Il Nuovo Cimento*, 12C(2), 173–209.
- Poirier, J., and C. D’Andrea (2002), Ground level muons in coincidence with the solar flare of 15 April 2001, *J. Geophys. Res.*, 107(A11), 1376, doi:10.1029/2001JA009187.
- Potgieter, M. S., H. Moraal, B. C. Raubenheimer, and P. H. Stoker (1980), Modulation of cosmic rays during solar minimum. III. Comparison of the latitude distributions for the periods of solar minimum during 1954, 1965 and 1976, *S. Afr. J. Phys.*, 3(3–4), 90–94.
- Raubenheimer, B. C., and P. H. Stoker (1974), Various aspects of the attenuation coefficient of a neutron monitor, *J. Geophys. Res.*, 79, 5069–5076.
- Stoker, P. H., and H. Moraal (1995), Neutron monitor latitude surveys at aircraft altitudes, *Astrophys. Space Sci.*, 230, 365–373.
- Stozhkov, Y. I., et al. (2009), Long-term (50 years) measurements of cosmic-ray fluxes in the atmosphere, *Adv. Space Res.*, 44, 1124–1137.
- Webber, W. R. and J. A. Lockwood (2001), Voyager and Pioneer spacecraft measurements of cosmic-ray intensities in the outer heliosphere—Toward a new paradigm for understanding the global modulation process: 1. Minimum solar modulation (1987 and 1997), *J. Geophys. Res.*, 106(A12), 29,333–29,340, doi:10.1029/2001JA000119.
- Webber, W. R. and P. R. Higbie (2010), What Voyager cosmic-ray data in the outer heliosphere tells us about ^{10}Be production in the Earth’s polar atmosphere in the recent past, *J. Geophys. Res.*, 115, A05102, doi:10.1029/2009JA014532.